# Topological Hall effect in frustrated B2-ordered $Mn_{0.74}Co_{0.57}Al_{0.69}$ films

Peng Chen, Chunlei Zhang, Yongzuo Wang, Bing Lv, Pei Liu, Yinhua Tian, Jiaqi Ran, Cunxu Gao,* Qingfang Liu,† and Desheng Xue‡

*Key Laboratory for Magnetism and Magnetic Materials of the Ministry of Education, Lanzhou University, 730000 Lanzhou, People's Republic of China*

(Received 22 January 2021; revised 17 June 2021; accepted 22 July 2021; published 5 August 2021)

Exploring materials with topological magnetic structures has always been the subject of intense research due to fundamental and technological interests. Here we report the topological Hall effect in the frustrated B2-ordered $Mn_{0.74}Co_{0.57}Al_{0.69}$ thin films. A large topological Hall resistivity of 58.3 nΩ cm is found at 300 K. It is shown that a spin reorientation transition occurs around 200 K through the temperature-dependent magnetization and angular-dependent ferromagnetic resonance measurements. Using the obtained magnetic anisotropy parameters, we perform the micromagnetic simulations to simulate the formation and evolution of topological magnetic structures with temperature, demonstrating the influence of the higher-order magnetic anisotropies. This work enriches the variety of materials exhibiting topological Hall effect and helps to clarify the mechanism of new emergent topological features in magnetic materials.

DOI: 10.1103/PhysRevB.104.064409

Topological Hall effect, one of the most studied topological transport phenomena in condensed matter physics, arises from the accumulated Berry phase when conduction electrons move through chiral spin textures, such as skyrmions [1–3]. Over the last decade, the topological Hall effect has been studied in a number of noncentrosymmetric magnetic materials, such as B20-ordered MnSi [4], FeGe [5,6], tetragonal Heusler alloys $Mn_2RhSn$ [7], $Mn_{1.5}PtSn$ [8,9], and interfacial symmetry-breaking heterostructures $SrIrO_3/SrRuO_3$ [10], where the Dzyaloshinsky-Moriya interaction stabilizes skyrmions. In addition, the topological Hall effect has also been found in a class of centrosymmetric crystals that do not involve Dzyaloshinsky-Moriya interaction, such as EuO [11], hexagonal MnNiGa [12], and frustrated $Mn_3Sn$ [13], $Fe_3Sn_2$ [14], $Gd_2PdSi_3$ [15]. It is found that the perpendicular magnetic anisotropy, magnetic frustration, and spin reorientation transition in these magnetic materials play a critical role in the formation of magnetic bubbles and skyrmions [16–19]. Recent theoretic studies have also shown that in frustrated materials with uniaxial anisotropy, skyrmions with additional degrees of freedoms of helicity and vorticity can be formed, which provides an opportunity to investigate their intriguing dynamics under external stimuli [20–22]. Therefore, exploring the emergent electrodynamics in magnetically frustrated centrosymmetric materials and clarifying their physical origins have become one of the challenging tasks in condensed matter physics.

Mn-Co-Al ternary alloys have been extensively studied because of its rich magnetic properties [23–30]. In 1962, Tsuboya *et al.* reported a new magnetic phase in ternary alloy systems Mn-Co-Al, named $\kappa$ phase [23]. However, since then, it seems not much effort has been made in new magnetic phase research. In 2010, Paduani *et al.* investigated the magnetic frustration behavior in the $\kappa$ phase Mn-Co-Al alloys [24]. This result brought us a challenge to realize topological magnetic structures and resultant topological Hall effect in the Mn-Co-Al ternary alloys through an off-stoichiometric modulation. In this work we present the observation of topological Hall effect in the frustrated B2-ordered $Mn_{0.74}Co_{0.57}Al_{0.69}$ (MCA) films grown on MgO(001) substrate, whose composition is close to the previously reported $\kappa$ phase. Our magnetic and transport measurements provide evidence for the existence of magnetic frustration and spin reorientation transition behaviors in the MCA films. After quantitatively characterizing the magnetic anisotropy of the MCA films, we found the topological Hall effect could be ascribed to the competition between magnetocrystalline anisotropy and demagnetization energy. Based on the experimentally obtained magnetic anisotropies, our micromagnetic simulations further confirmed the spin reorientation transition process as the temperature decreases [from out-of-plane (OOP) to in-plane (IP) direction]. In addition, it is found that the topological magnetic structures, such as magnetic bubbles and bimerons, could be successfully formed above the transition temperature, which can cause topological Hall effect in the MCA films.

The Mn-Co-Al films were epitaxially grown on MgO(001) substrates by a custom-built molecular-beam epitaxy system. Prior to growth, the MgO substrate was cleansed according to the methods described in Ref. [31]. A 0.3-nm-thick CoAl buffer layer was first deposited at 200 °C, then the substrate temperature was raised to 500 °C and annealed for 10 min. Subsequently, the substrate temperature was reduced to 350 °C and the MCA growth was occurred to a thickness of 24.4 nm. Finally, a 3-nm-thick Al was capped to prevent oxidation in air. Nucleation and growth were monitored *in situ* by reflection high-energy electron diffraction (RHEED). The atomic rate of Mn, Co, Al sources were calibrated by

*gaocunx@lzu.edu.cn
†liuqf@lzu.edu.cn
‡xueds@lzu.edu.cn

 

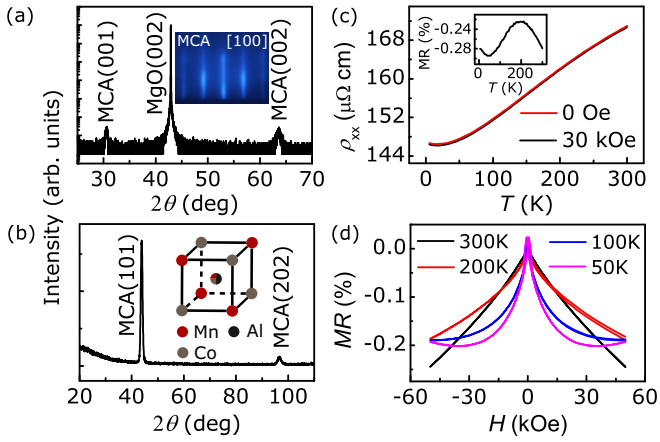


FIG. 1. (a) Symmetrical $\theta$-$2\theta$ pattern of the MCA on MgO(001) substrate. The inset shows the stationary RHEED patterns of the MCA films along their [100] azimuths. (b) The asymmetrical $\omega$-$2\theta$ scan of the (101) plane. The inset shows the B2 configuration containing Mn, Co, and Al atoms schematically. (c) Temperature dependence of the resistivity of the MCA measured with zero magnetic field and 30 kOe, respectively. The inset shows the temperature dependence of magnetoresistivity under a magnetic field of 30 kOe. (d) Magnetic-field dependent magnetoresistivity measured at different temperatures with the magnetic field applied perpendicular to the surface of the MCA films.

x-ray reflectivity measurements, respectively. The film composition was determined to be $Mn_{0.74}Co_{0.57}Al_{0.69}$. The crystal structure and orientation of the samples were assessed by high-resolution x-ray diffraction (HRXRD). Magnetic characterizations including magnetization-field ($M$-$H$) curves and magnetization-temperature ($M$-$T$) curves were obtained from the superconducting quantum interference device (SQUID). The films were patterned into Hall bar by photolithography (120 $\mu$m long $\times$ 20 $\mu$m wide) and Ar ion milling for transport measurements. The transport measurements were performed on a physical property measurement system (PPMS, Quantum Design Inc., San Diego, USA). The raw Hall resistivity was antisymmetrized to exclude the contribution from longitudinal magnetoresistance. OOP ferromagnetic resonance (FMR) measurements were performed in an electron spin resonance spectrometer ($X$ band at 8.969 GHz, JES-FA 300, JEOL). Micromagnetic simulations were performed using the GPU-accelerated micromagnetic simulation software MuMax$^3$ based on the Landau-Lifshitz-Gilbert (LLG) function. The energy terms include the exchange interaction, tetragonal magnetocrystalline anisotropy, demagnetization, and Zeeman energy.

The crystal structure and lattice parameters were obtained from the HRXRD measurements. XRD symmetric $\theta$-$2\theta$ scan was recorded with an analyzer, while asymmetrical $\omega$-$2\theta$ scan was taken with an open detector. Figure 1(a) shows the symmetrical HRXRD $\theta$-$2\theta$ scans of the films on MgO(001) substrate. In addition to the (002) reflection of MgO, the (001) and (002) reflections of MCA are clearly observed, demonstrating the epitaxial growth of the films along the (001) orientation. The calculated experimental intensity ratio $I_{001}/I_{002}$ is 0.68, which is close to the theoretical value of 0.77. Thus, the clear (001) peak indicates the well-ordered arrangement of Al, and Mn or Co [23,32] (see details in the Supplemental Material [33], see, also, Refs. [34–36] therein). The OOP lattice constant obtained by the MCA(002) reflection is 2.93 Å. The inset of Fig. 1(a) shows the stationary RHEED patterns of the MCA films along their [100] azimuths. The elongated strips evidence a high-quality epitaxial growth of MCA films. An asymmetrical $\omega$-$2\theta$ was also performed for a (202) plane with $\chi = 45^\circ$, as shown in Fig. 1(b). The IP lattice constant is determined to be 2.91 Å, which is approximately the same as the OOP one. Thus, the MCA films have the body-centered cubic structure of B2 type (CsCl type). A thickness of 24.4 nm is deduced from the x-ray reflectivity (XRR) measurements (Fig. S1, Supplemental Material [33]). The inset of Fig. 1(b) shows the B2 configuration containing Mn, Co, and Al atoms schematically. For the off-stoichiometric $Mn_{0.74}Co_{0.57}Al_{0.69}$ films, we believe that the Mn and Co atoms occupy cube corner site almost equally, and the excess Mn and Co atoms are considered to enter into the body center sites together with the Al atoms. It is well known that the ferromagnetic or antiferromagnetic exchange interaction of Co-Mn and Mn-Mn strongly depends on the distance between atoms [24,32,37,38]. For instance, when the atomic distance is shorter than about 2.8 Å, the magnetic interaction between nearest-neighbor Mn atoms is antiferromagnetic, and if the distance is greater than about 2.9 Å, it is ferromagnetic [24,32]. Therefore, if we consider the atomic disorder between Mn and Co, there is a coexistence of ferromagnetic and antiferromagnetic interactions, which may induce frustration behavior in our MCA films. Figure 1(c) presents the resistivity $\rho_{xx}$ as a function of temperature $T$, where magnetic field $H$ is applied along the OOP direction for $H = 0$ Oe and $H = 30$ kOe, respectively. The temperature-dependent resistivity demonstrates a metallic behavior but with a small residual resistivity ratio of about 1.2, revealing a highly disordered atomic arrangement between Mn and Co. The inset of Fig. 1(c) shows the temperature dependence of magnetoresistance (MR) (MR $= [\rho(H) - \rho(0)]/\rho(0)$). In addition to the temperature-dependent minimum value at around 50 K, which can be ascribed to the three-dimensional electron-electron interaction in disordered metals [31], the maximum value of MR can be clearly observed around 200 K. This may indicate the magnetic transition because of the competition of ferromagnetic-antiferromagnetic interactions in MCA. Figure 1(d) depicts the magnetic field dependent MR, which exhibits small hysteresis behaviors.

To study the possible topological magnetic structures in MCA, we now turn to the Hall effect measurements. Generally, the Hall resistivity can be expressed as [4]

$$\rho_{xy} - R_0 H = a\rho_{xx0} M + S_A \rho_{xx}^2 M + \rho_{xy}^T, \qquad (1)$$

where $R_0$, $a\rho_{xx0}M$, $S_A\rho_{xx}^2 M$, and $\rho_{xy}^T$ correspond to the ordinary Hall coefficients, the anomalous Hall contribution originating from the skew-scattering mechanism, the anomalous Hall contribution originating from the side-jump and intrinsic mechanism, and topological Hall resistivity, respectively. Here $M$ is the OOP magnetization. Figure 2(a) shows the magnetic field dependence of Hall resistivity after subtraction of ordinary Hall effect for 50–300 K at magnetic fields

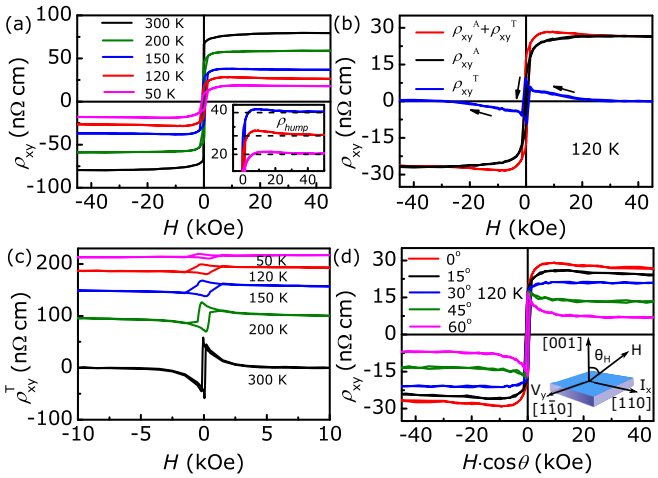


FIG. 2. (a) Hall resistivity of the $Mn_{0.74}Co_{0.57}Al_{0.69}$ films after subtraction of ordinary Hall effect at different temperatures. The inset shows the Hall resistivity in the range of 10–40 nΩ cm. Definitions of $\rho_{hump}$ are indicated by the black dashed lines. (b) The process of extracting anomalous Hall resistivity ($\rho_{xy}^A$) and topological Hall resistivity ($\rho_{xy}^T$) at 120 K. The black arrows represent the the direction of the magnetic field scan. (c) Magnetic field dependence of topological Hall resistivity $\rho_{xy}^T$ obtained at different temperatures, which are plotted with an arbitrary offset for clarity. (d) Magnetic field dependence of the Hall resistance after subtraction of ordinary Hall effect at various inclination angles. In the inset it shows the schematic of the measurement configuration. The inclination angle $\theta_H$ is defined as the angle between the film normal and the magnetic field. The IP direction of the applied magnetic field is fixed along the MCA[110] in our experiments.

up to 50 kOe. It can be seen that an enhanced Hall signal $\rho_{hump}$ ($\rho_{peak}$-$\rho_{xy}^A$) appears in the low-field region of the Hall curves below the transition temperatures of around 200 K, indicating the presence of topological magnetic structures at low temperatures [7–9]. According to the interpretation of the superposition model with opposite anomalous Hall resistivity polarity, $\rho_{hump}$ should reach the maximum value when the sign of the anomalous Hall resistivity $\rho_{xy}^A$ reverses [39,40]. However, the temperature-dependent anomalous Hall resistivity $\rho_{xy}^A$ does not have a sign reversal (Fig. S2, Supplemental Material [33]). As shown in the inset of Fig. 2(a), the Hall resistivity anomaly $\rho_{hump}$ reaches a maximum value at a intermediate temperature of 120 K, which is not consistent with the inhomogeneous magnetization model. Thus, we believe that the inhomogeneous magnetism model can be ruled out in our case. To extract topological Hall resistivity arising from topological magnetic structures, we take the Hall resistivity data measured at 120 K as a representative example to illustrate the procedures. As the skew-scattering mechanism basically is dominant in the high-conductivity regime ($\sigma_{xx} \geqslant 10^6\ \Omega^{-1}\,cm^{-1}$) [41], it can be safely ruled out for the MCA films ($\sim 10^4\ \Omega^{-1}\,cm^{-1}$). In addition, the MCA films show very small magnetoresistance ($< 0.3\%$ at fields up to 50 kOe), and we anticipate that $S_A$ is an H-independent parameter. Thus $S_A\rho_{xx}^2$ is approximately magnetic field independent. Considering that the topological Hall contribution is absent at high fields, $R_0$ and $S_A\rho_{xx}^2$ can be obtained from the linear fit to the plot of $\rho_{xy}/H$ vs $M/H$, and then used to reconstruct the ordinary Hall effect and anomalous Hall effect throughout the whole field range (Fig. S3, Supplemental Material [33]). As shown in Fig. 2(b), the red curve corresponds to ($\rho_{xy}$-$R_0H$) and the black curve represents the fitted anomalous Hall resistivity $\rho_{xy}^A$. Then, a nonzero $\rho_{xy}^T$ is obtained at low fields shown in blue solid curve. When the field sweeps from +50 to −50 kOe, it can be seen that $\rho_{xy}^T$ first exhibits a positive maxima of 9.4 nΩ cm for field of about −0.2 kOe. Then it suddenly falls to a negative value of −6.0 nΩ cm for a field of about −1.5 kOe and finally increases to zero. The sign change of $\rho_{xy}^T$ can be regarded as the signatures of topological Hall resistivity [1,6,42,43]. We have performed similar analysis for the temperatures between 300 and 50 K and the extracted topological Hall resistivity is presented in Fig. 2(c). As the temperature increases, $\rho_{xy}^T$ continues to increase, indicating the enhancement of the topological Hall effect. The magnitude of $\rho_{xy}^T$ obtained at 300 K is about 58.3 nΩ cm, which is much larger than that obtained in the $Mn_2CoAl$/Pd films (7 nΩ cm) [25].

Generally, when the magnetic field deviates from the normal direction of the films, the two-dimensional skyrmions stabilized by the Dzyaloshinsky-Moriya interaction will be destroyed [11,44,45]. So, the topological Hall resistivity would disappear under a tilt of magnetic field. To study the evolution of possible skyrmion phase with external magnetic field, we measured the magnetic field dependence of Hall resistivity with various inclination angles $\theta_H$. The inset of Fig. 2(d) depicts the inclination angle $\theta_H$ schematically. Figure 2(d) presents the magnetic-field dependence of the Hall resistivity curves obtained at various inclination angles at 120 K up to 90 kOe. As expected, when $\theta_H$ increases from 0° to 30°, the humplike structure in $\rho_{xy}$ gradually disappears in the low field region of the curves. However, when $\theta_H$ continuously increases from 30° to 60°, a cusplike structure emerges and even gets larger at higher inclination angles, indicating that the topological magnetic structure can exist in a tilt of magnetic field. Similar cusplike behaviors were reported in several magnetic frustrated materials, such as $Pr_2Ir_2O_7$ [46], $PdCrO_2$ [47], and $Fe_3GeTe_2$ films [48,49], in which the Hall resistivity anomalies are attributed to the appearance of noncollinear spin structures when magnetic field is tilted away from the uniaxial magnetic axis. Therefore, our results suggest that the topological magnetic structures could be stabilized even when the magnetic field is tilted in the MCA thin films. However, compared with the tetragonal $Mn_{1.5}PtSn$ [8,9] or $Mn_2CoAl$/Pd [25] films, the lack of heavy metal make the Dzyaloshinsky-Moriya interaction an unlikely source of these topological spin textures. Our Brillouin light scattering (BLS) measurements also show that there is indeed no Dzyaloshinsky-Moriya interaction in the MCA films (Fig. S5, Supplemental Material [33], see, also, Refs. [50–53], therein). On the other hand, recent studies show that the magnetic anisotropy plays a pivotal role for the formations of skyrmions in the frustrated magnetic systems [21,22,54]. Thus, to understand the origins of the topological spin structures in the MCA films, we need to investigate its magnetic anisotropy.

We first measured the OOP and IP hysteresis loops from 300–50 K. The diamagnetic signal of the substrate were determined from the high-field linear part of the original data

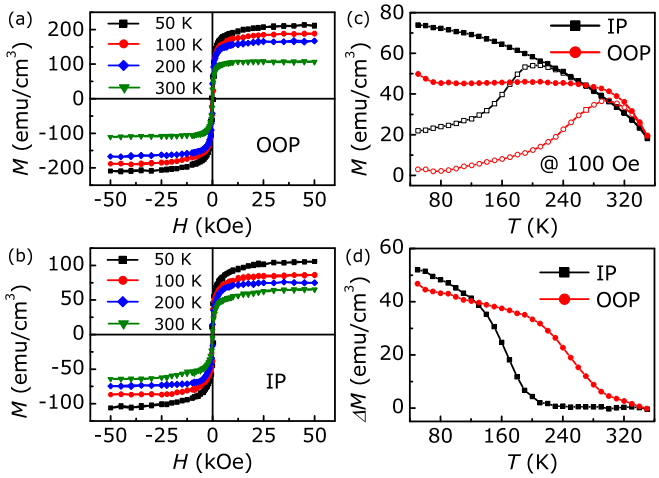


FIG. 3. (a) The OOP hysteresis loops measured at 50, 100, 200, and 300 K, respectively. (b) The IP hysteresis loops measured at 50, 100, 200, and 300 K, respectively. (c) Temperature dependence of ZFC and FC magnetization measured under $H = 100$ Oe with $H \parallel$ MCA [110] and $H \parallel$ MCA [001]. Open symbols correspond to the ZFC and closed symbols to FC branch. (d) Variation of magnetization $\Delta M$ ($M_{FC}$-$M_{ZFC}$) versus temperature.

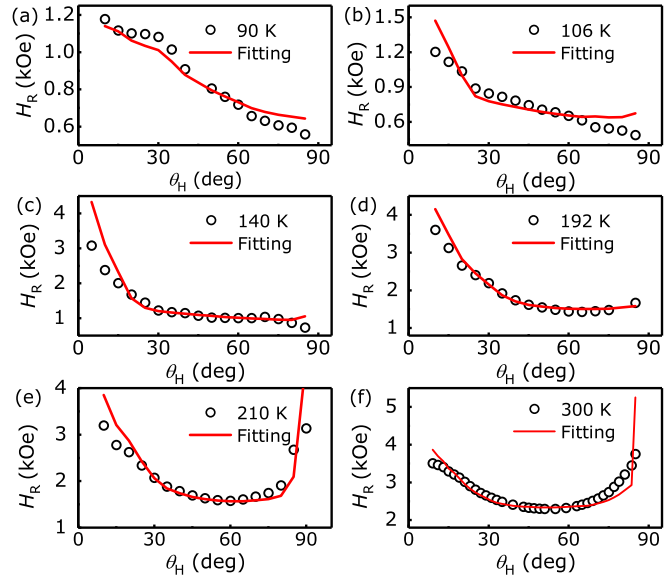


FIG. 4. Polar angle $\theta_H$ dependence of the resonance field $H_R$ for MCA films at (a) 90 K, (b) 106 K, (c) 140 K, (d) 192 K, (e) 210 K, and (f) 300 K, respectively.

and were subtracted. Figure 3(a) shows the OOP magnetization curves measured between 300 and 50 K. Unlike the magnetic phase diagram reported by Tsuboya *et al.* [23], the MCA films exhibit a small magnetization ($M_s$), reaching up to 210 emu/cm$^3$ at 50 K, which may be attributed to the good crystallinity. Moreover, as the temperature decreases from 300 to 50 K, the OOP hysteresis loop becomes more difficult to saturate, revealing that magnetic anisotropy has changed. As a comparison, Fig. 3(b) shows the IP magnetization curves measured between 300 and 50 K. We measured the temperature dependence of magnetization $M(T)$ from 350 to 50 K with zero-field-cooled (ZFC) and field-cooling (FC) modes to further characterize the magnetic properties in MCA films. Figure 3(c) shows a divergence of the ZFC and FC $M(T)$ curves measured under an IP and OOP magnetic field of 100 Oe, signifying the presence of competing magnetic interactions in the MCA films. A similar result was also reported in previous bulk Mn-Co-Al alloys [24]. We plot the FC-ZFC magnetization difference ($\Delta M$) in Fig. 3(d). The $\Delta M$ value remains almost zero down to 200 K, and then increases abruptly for the IP case. On the other hand, for the OOP case, the $\Delta M$ value increases rapidly from 350 to 200 K, but increases slowly below 200 K. These results indicate that the MCA may undergo a spin reorientation transition from OOP to IP direction around 200 K [13,43,55]. The Curie temperature ($T_c$) determined by the OOP $M(T)$ curve is 457 K, demonstrating the potential for applications in future spintronic devices (Fig. S6, Supplemental Material [33]).

To investigate the magnetic anisotropy quantitatively, we measured their OOP angular dependence of ferromagnetic resonance at various temperatures ranging from 300 K to 90 K. Typical FMR spectrum were presented in Fig. S7 (Supplemental Material [33]). Figure 4 shows the resonance field $H_R$ as a function of inclination angle $\theta_H$ from 300 to 90 K, where $\theta_H$ is defined in the inset of Fig. 2(d). One can see that easy axis is inclined between [110] and [001] directions at 300 and 210 K, whereas the easy axis has turned into IP directions from 192 to 90 K. These results reveal that the MCA films have experienced a spin reorientation transition at around 200 K, which are consistent with our temperature-dependent magnetization measurements. A similar complex magnetic magnetocrystalline anisotropy was also reported in the $SrRuO_3$ films [56]. It should be noted that the topological magnetic structures can be formed in magnetic materials near their spin reorientation transition temperatures, such as $Fe_3Sn_2$ [18], $Nd_2Fe_{14}B$ [19], Cu-substituted MnNiGa [57], $La_{2-2x}Sr_{1-2x}Mn_2O_7$ [58], and Fe/Ni/Cu(001) multilayers [59]. Considering the constraints of $\frac{\partial^2 F}{\partial \theta^2} > 0$ ($F$ is the total free-energy density), $H_R$ as a function of $\theta_H$ were calculated numerically using Eqs. (2) and (3) (see details in the Supplemental Material [33], see, also, Refs. [60–63], therein),

$$\sin(\theta_H - \theta) = -\frac{\sin 2\theta}{H_R}\left\{\left(2\pi M_s - \frac{K_2}{M_s} - \frac{K_{4\perp}}{M_s}\right) + \sin^2\theta\left(\frac{K_{4\perp}}{M_s} + \frac{K_{4\parallel}}{2M_s}\right)\right\}, \tag{2}$$

$$\left(\frac{\omega}{\gamma}\right)^2 = \left\{H_R\cos(\theta_H - \theta) + \left(-4\pi M_s + \frac{2K_2}{M_s} + \frac{K_{4\perp}}{M_s} - \frac{K_{4\parallel}}{2M_s}\right)\cos 2\theta + \left(\frac{K_{4\perp}}{M_s} + \frac{K_{4\parallel}}{2M_s}\right)\cos 4\theta\right\}$$
$$\times\left\{H_R\cos(\theta_H - \theta) + \left(-4\pi M_s + \frac{2K_2}{M_s} + \frac{K_{4\parallel}}{M_s}\right)\cos^2\theta + \left(\frac{2K_{4\perp}}{M_s} + \frac{K_{4\parallel}}{M_s}\right)\cos^4\theta - \frac{2K_{4\parallel}}{M_s}\right\}, \tag{3}$$

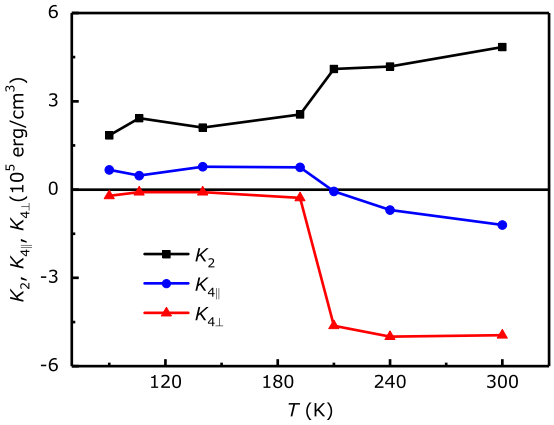


FIG. 5. The temperature-dependent $K_2$, $K_{4\perp}$, and $K_{4\|}$, respectively.

where $\omega$ is the circular frequency, $\gamma$ is the gyromagnetic ratio, and $\theta$ is the polar angles of the magnetization $M_s$. $K_2$, $K_{4\perp}$, and $K_{4\|}$ are the perpendicular anisotropy energy, OOP, and IP fourfold magnetocrystalline anisotropy energy, respectively. Figure 5 shows the fitted $K_2$, $K_{4\perp}$, and $K_{4\|}$ as a function of temperature. It can be seen that $K_2$ varies slightly from $4.85 \times 10^5$ erg/cm$^3$ at 300 K to $1.84 \times 10^5$ erg/cm$^3$ at 90 K. The perpendicular anisotropy energy $K_2$ obtained here is comparable to the demagnetization field energy $2\pi M_s^2$ ($2.8 \times 10^5$ erg/cm$^3$). According to previous studies, when perpendicular anisotropy energy exceeds the demagnetization field energy, a uniaxial ferromagnet of finite thickness spontaneously breaks into parallel "striped" domains as a result of demagnetizing forces [64]. When a magnetic field is applied out-of-plane, domains with an antiparallel magnetization shrink until they break into roughly circular domains called magnetic bubbles. The magnetization gradually rotates within the domain wall region, and the rotating behavior defines the two degrees of freedom, i.e., helicity and vorticity. Thus, a magnetic bubble can be regarded as a skyrmion in a broad sense and is called a "skyrmionic bubble," which can also cause topological Hall effect [17,65–67]. Noticing that recent micromagnetic simulations of thin films also show that topological magnetic states can be formed by an applied magnetic field even for $Q < 1$, where $Q$ is equal to the ratio of perpendicular magnetic anisotropy to demagnetization energy [54,68]. Therefore, considering the spin reorientation transition and large perpendicular anisotropy in the frustrated MCA films, we attribute the observed topological Hall effect at low temperatures to the competition between the magnetocrystalline anisotropy and demagnetization energy, which may induce topological magnetic structures, such as magnetic bubbles or skyrmions.

Micromagnetic simulations were performed to confirm the mechanism stabilizing topological magnetic structures using the experimentally obtained parameters. The initial magnetization vector states are randomly distributed. Model size is $900 \times 900 \times 24$ nm$^3$, which is divided into $300 \times 300 \times 8$ meshes. The exchange constant $A$ and the magnetization $M_s$ are set as $1.5 \times 10^{-11}$ J/m and 210 emu/cm$^3$, respectively. The experimentally obtained magnetic anisotropies $K_2$, $K_{4\|}$, and $K_{4\perp}$ are converted to $K_1'$, $K_2'$, and $K_3'$ for micromagnetic simulations according to $K_1' = K_2 - K_{4\|}$, $K_2' = (K_{4\perp} + K_{4\|})/2$, $K_3' = -K_{4\|}$, respectively (see more details in Fig. S8, Supplemental Material [33], see, also, Refs. [69–72], therein). As shown in Fig. 6, our simulations show that the magnetic moment undergoes a spin reorientation transition from IP to OOP when the temperature rises. Importantly, the topological magnetic structures, such as magnetic bubbles and bimerons, could be successfully formed above the spin reorientation transition temperature. We believe that these magnetic structures can give rise to topological Hall effect [73,74]. There is no topological magnetic structure below 192 K, which is different from the Hall effect measurement at low temperatures. We speculate that defects and imperfections in the experiment may cause these deviations, which are not considered in the micromagnetic simulations. In Fig. S9 the evolution

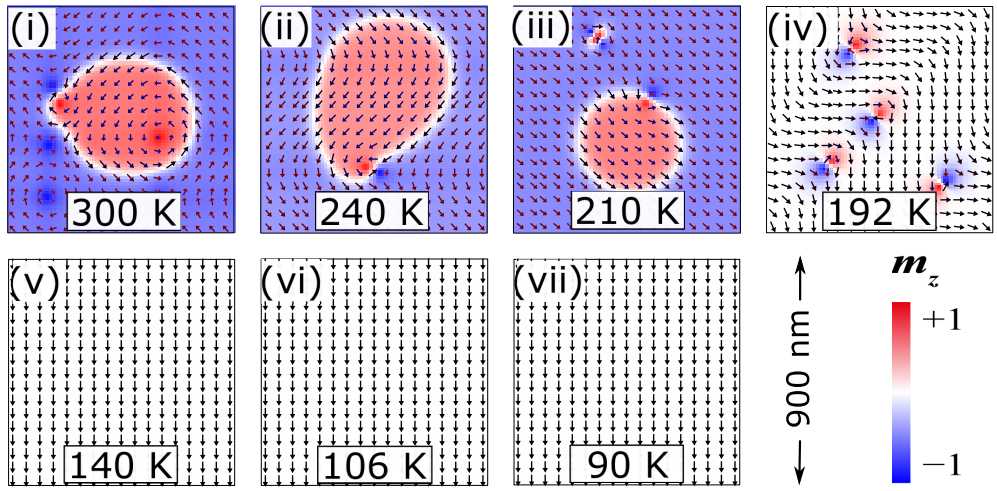


FIG. 6. The temperature evolution of magnetic structures from 300 to 90 K. The input magnetic anisotropy parameters including $K_1'$, $K_2'$, and $K_3'$ are derived from the experimentally obtained magnetic anisotropies $K_2$, $K_{4\perp}$, and $K_{4\|}$, respectively. The model size is $900 \times 900 \times 24$ nm$^3$, which is divided into $300 \times 300 \times 8$ meshes. The arrow denotes the IP spin components ($m_x$, $m_y$), and the color scale represents the OOP spin component ($m_z$).

of the magnetic bubbles was also investigated under the action of a magnetic field. It can be seen that the topology of magnetic bubbles can be changed under an application of magnetic field, which led to the sign change in the topological Hall resistivity [1,44]. In addition, it is shown that the topological magnetic structures stabilized by magnetocrystalline anisotropy can be stabilized in a tilted magnetic field, which is quite different from the skyrmions stabilized by the Dzyaloshinky-Moriya interaction (Fig. S10, Supplemental Material [33]).

In conclusion, epitaxial $Mn_{0.74}Co_{0.57}Al_{0.69}$ films with B2-ordered structure were grown on MgO(001) substrate. Our magnetic and transport measurements provide evidence for the existence of magnetic frustration and spin reorientation transition at low temperatures in the MCA films. A large perpendicular magnetic anisotropy energy $K_2$ of $4.85 \times 10^5$ erg/cm$^3$ is obtained at 300 K through a fitting of the OOP angle-dependent resonance fields. We attribute the observed topological Hall effect to the emergence of topological magnetic structures (such as magnetic bubbles and bimerons) caused by the competition between magnetocrystalline anisotropy and demagnetization energy in the MCA films. The formation and evolution of topological magnetic structures are further confirmed by the micromagnetic simulations. This work enriches the materials exhibiting topological Hall effect and paves the way to study the intriguing skyrmion dynamics in the magnetically frustrated alloys.

We are indebted to Tao Zhu at the Chinese Academy of Sciences for insightful discussions. This work was supported by the National Natural Science Foundation of China (Grants No. 11674141, No. 12074158, No. 12074157, and No. 91963201), 111 Project (Grant No. B20063), PCSIRT (Grant No. IRT 16R35), and Natural Science Foundation of Gansu Province (Grant No. 20JR5RA291).

[1] P. Bruno, V. K. Dugaev, and M. Taillefumier, Phys. Rev. Lett. **93**, 096806 (2004).
[2] M. Onoda, G. Tatara, and N. Nagaosa, J. Phys. Soc. Jpn. **73**, 2624 (2004).
[3] K.-W. Kim, H.-W. Lee, K.-J. Lee, and M. D. Stiles, Phys. Rev. Lett. **111**, 216601 (2013).
[4] Y. Li, N. Kanazawa, X. Z. Yu, A. Tsukazaki, M. Kawasaki, M. Ichikawa, X. F. Jin, F. Kagawa, and Y. Tokura, Phys. Rev. Lett. **110**, 117202 (2013).
[5] S. X. Huang and C. L. Chien, Phys. Rev. Lett. **108**, 267201 (2012).
[6] J. C. Gallagher, K. Y. Meng, J. T. Brangham, H. L. Wang, B. D. Esser, D. W. McComb, and F. Y. Yang, Phys. Rev. Lett. **118**, 027201 (2017).
[7] K. Rana, O. Meshcheriakova, J. Kübler, B. Ernst, J. Karel, R. Hillebrand, E. Pippel, P. Werner, A. Nayak, C. Felser *et al.*, New J. Phys. **18**, 085007 (2016).
[8] P. Swekis, A. Markou, D. Kriegner, J. Gayles, R. Schlitz, W. Schnelle, S. T. B. Goennenwein, and C. Felser, Phys. Rev. Mater. **3**, 013001(R) (2019).
[9] V. Kumar, N. Kumar, M. Reehuis, J. Gayles, A. S. Sukhanov, A. Hoser, F. Damay, C. Shekhar, P. Adler, and C. Felser, Phys. Rev. B **101**, 014424 (2020).
[10] J. Matsuno, N. Ogawa, K. Yasuda, F. Kagawa, W. Koshibae, N. Nagaosa, Y. Tokura, and M. Kawasaki, Sci. Adv. **2**, e1600304 (2016).
[11] Y. Ohuchi, Y. Kozuka, M. Uchida, K. Ueno, A. Tsukazaki, and M. Kawasaki, Phys. Rev. B **91**, 245115 (2015).
[12] B. Ding, Y. Li, C. Xu, Y. Wang, Z. Hou, E. Liu, Z. Liu, G. Wu, and W. Wang, Appl. Phys. Lett. **110**, 092404 (2017).
[13] P. K. Rout, PrakashP. V. Madduri, S. K. Manna, and A. K. Nayak, Phys. Rev. B **99**, 094430 (2019).
[14] H. Li, B. Ding, J. Chen, Z. Li, Z. Hou, E. Liu, H. Zhang, X. Xi, G. Wu, and W. Wang, Appl. Phys. Lett. **114**, 192408 (2019).
[15] T. Kurumaji, T. Nakajima, M. Hirschberger, A. Kikkawa, Y. Yamasaki, H. Sagayama, H. Nakao, Y. Taguchi, T. Arima, and Y. Tokura, Science **365**, 914 (2019).
[16] X. Yu, M. Mostovoy, Y. Tokunaga, W. Zhang, K. Kimoto, Y. Matsui, Y. Kaneko, N. Nagaosa, and Y. Tokura, Proc. Natl. Acad. Sci. **109**, 8856 (2012).
[17] W. Wang, Y. Zhang, G. Xu, L. Peng, B. Ding, Y. Wang, Z. Hou, X. Zhang, X. Li, and E. Liu, Adv. Mater. **28**, 6887 (2016).
[18] Z. Hou, W. Ren, B. Ding, G. Xu, Y. Wang, B. Yang, Q. Zhang, Y. Zhang, E. Liu, and F. Xu, Adv. Mater. **29**, 1701144 (2017).
[19] Y. Xiao, F. Morvan, A. He, M. Wang, H. Luo, R. Jiao, G. Zhao, and J. Liu, Appl. Phys. Lett. **117**, 132402 (2020).
[20] T. Okubo, S. Chung, and H. Kawamura, Phys. Rev. Lett. **108**, 017206 (2012).
[21] S.-Z. Lin and S. Hayami, Phys. Rev. B **93**, 064430 (2016).
[22] X. Zhang, J. Xia, Y. Zhou, X. Liu, H. Zhang, and M. Ezawa, Nat. Commun. **8**, 1717 (2017).
[23] I. Tsuboya and M. Sugihara, J. Phys. Soc. Jpn. **17**, 410 (1962).
[24] C. Paduani, J. Schaf, A. I. C. Persiano, J. D. Ardisson, A. Y. Takeuchi, and I. C. Riegel, Intermetallics **18**, 1659 (2010).
[25] B. Ludbrook, G. Dubuis, A.-H. Puichaud, B. Ruck, and S. Granville, Sci. Rep. **7**, 13620 (2017).
[26] R. Kainuma, M. Ise, K. Ishikawa, I. Ohnuma, and K. Ishida, J. Alloys Compd. **269**, 173 (1998).
[27] H. Shiraishi, T. Hori, and Y. Yamaguchi, J. Magn. Magn. Mater. **104**, 2040 (1992).
[28] J. Kübler and C. Felser, Europhys. Lett. **114**, 47005 (2016).
[29] S. Ouardi, G. H. Fecher, C. Felser, and J. Kübler, Phys. Rev. Lett. **110**, 100401 (2013).
[30] P. Li, J. Koo, W. Ning, J. Li, L. Miao, L. Min, Y. Zhu, Y. Wang, N. Alem, Z. Liu, C. Mao, and B. Yan, Nat. Commun. **11**, 4769 (2020).
[31] P. Chen, C. Gao, G. Chen, K. Mi, M. Liu, P. Zhang, and D. Xue, Appl. Phys. Lett. **113**, 122402 (2018).
[32] I. Tsuboya, J. Phys. Soc. Jpn. **16**, 1875 (1961).
[33] See Supplemental Material at http://link.aps.org/supplemental/10.1103/PhysRevB.104.064409 for details of x-ray intensity analysis, physical property measurements, FMR fittings, and micromagnetic simulations.
[34] J. Connolly, *Diffraction Basics II: Intensities* (2012) https://www.slideserve.com/lainey/diffraction-basics-ii-intensities.

[35] L. Bainsla, R. Yilgin, J. Okabayashi, A. Ono, K. Suzuki, and S. Mizukami, Phys. Rev. B **96**, 094404 (2017).

[36] H. P. Hanson, F. Herman, J. D. Lea, and S. Skillman, Acta Crystallogr. **17**, 1040 (1964).

[37] L. Feng, L. Ma, Z. Y. Zhu, W. Zhu, E. K. Liu, J. L. Chen, G. H. Wu, F. B. Meng, H. Y. Liu, H. Z. Luo, and Y. X. Li, J. Appl. Phys. **107**, 013913 (2010).

[38] G. D. Liu, X. F. Dai, H. Y. Liu, J. L. Chen, Y. X. Li, G. Xiao, and G. H. Wu, Phys. Rev. B **77**, 014424 (2008).

[39] D. Kan, T. Moriyama, K. Kobayashi, and Y. Shimakawa, Phys. Rev. B **98**, 180408(R) (2018).

[40] A. Gerber, Phys. Rev. B **98**, 214440 (2018).

[41] N. Nagaosa, J. Sinova, S. Onoda, A. H. MacDonald, and N. P. Ong, Rev. Mod. Phys. **82**, 1539 (2010).

[42] M. He, G. Li, Z. Zhu, Y. Zhang, L. Peng, R. Li, J. Li, H. Wei, T. Zhao, X. G. Zhang, S. Wang, S.-Z. Lin, L. Gu, G. Yu, J. W. Cai, and B.-g. Shen, Phys. Rev. B **97**, 174419 (2018).

[43] B. Giri, A. I. Mallick, C. Singh, PrakashP. V. Madduri, F. Damay, A. Alam, and A. K. Nayak, Phys. Rev. B **102**, 014449 (2020).

[44] N. Kanazawa, M. Kubota, A. Tsukazaki, Y. Kozuka, K. S. Takahashi, M. Kawasaki, M. Ichikawa, F. Kagawa, and Y. Tokura, Phys. Rev. B **91**, 041122(R) (2015).

[45] T. Yokouchi, N. Kanazawa, A. Tsukazaki, Y. Kozuka, M. Kawasaki, M. Ichikawa, F. Kagawa, and Y. Tokura, Phys. Rev. B **89**, 064416 (2014).

[46] Y. Machida, S. Nakatsuji, Y. Maeno, T. Tayama, T. Sakakibara, and S. Onoda, Phys. Rev. Lett. **98**, 057203 (2007).

[47] H. Takatsu, S. Yonezawa, S. Fujimoto, and Y. Maeno, Phys. Rev. Lett. **105**, 137201 (2010).

[48] Y. Wang, C. Xian, J. Wang, B. Liu, L. Ling, L. Zhang, L. Cao, Z. Qu, and Y. Xiong, Phys. Rev. B **96**, 134428 (2017).

[49] Y. You, Y. Gong, H. Li, Z. Li, M. Zhu, J. Tang, E. Liu, Y. Yao, G. Xu, F. Xu, and W. Wang, Phys. Rev. B **100**, 134441 (2019).

[50] S. Demokritov, B. Hillebrands, and A. Slavin, Phys. Rep. **348**, 441 (2001).

[51] S. Seki, Y. Okamura, K. Kondou, K. Shibata, M. Kubota, R. Takagi, F. Kagawa, M. Kawasaki, G. Tatara, Y. Otani, and Y. Tokura, Phys. Rev. B **93**, 235131 (2016).

[52] H. T. Nembach, J. M. Shaw, M. Weiler, E. Jue, and T. J. Silva, Nat. Phys. **11**, 825 (2015).

[53] X. Ma, G. Yu, X. Li, T. Wang, D. Wu, K. S. Olsson, Z. Chu, K. An, J. Q. Xiao, K. L. Wang, and X. Li, Phys. Rev. B **94**, 180408(R) (2016).

[54] S. A. Montoya, S. Couture, J. J. Chess, J. C. T. Lee, N. Kent, D. Henze, S. K. Sinha, M. Y. Im, S. D. Kevan, P. Fischer, B. J. McMorran, V. Lomakin, S. Roy, and E. E. Fullerton, Phys. Rev. B **95**, 024415 (2017).

[55] J. Liu, S. Zuo, X. Zheng, Y. Zhang, T. Zhao, F. Hu, J. Sun, and B. Shen, Appl. Phys. Lett. **117**, 052407 (2020).

[56] M. Ziese, I. Vrejoiu, and D. Hesse, Phys. Rev. B **81**, 184418 (2010).

[57] G. Xu, Y. You, J. Tang, H. Zhang, H. Li, X. Miao, Y. Gong, Z. Hou, Z. Cheng, J. Wang, A. J. Studer, F. Xu, and W. Wang, Phys. Rev. B **100**, 054416 (2019).

[58] T. Asaka, T. Kimura, T. Nagai, X. Z. Yu, K. Kimoto, Y. Tokura, and Y. Matsui, Phys. Rev. Lett. **95**, 227204 (2005).

[59] J. Choi, J. Wu, C. Won, Y. Z. Wu, A. Scholl, A. Doran, T. Owens, and Z. Q. Qiu, Phys. Rev. Lett. **98**, 207205 (2007).

[60] H. Zabel and S. D. Bader, Eds., *Magnetic Heterostructures: Advances and Perspectives in Spinstructures and Spintransport* (Springer, Berlin, 2008), pp. 60–61.

[61] M. Farle, B. Mirwald-Schulz, A. N. Anisimov, W. Platow, and K. Baberschke, Phys. Rev. B **55**, 3708 (1997).

[62] H. Shul, Phys. Rev. **97**, 555 (1955).

[63] S. Akansel, A. Kumar, N. Behera, S. Husain, R. Brucas, S. Chaudhary, and P. Svedlindh, Phys. Rev. B **97**, 134421 (2018).

[64] T. Garel and S. Doniach, Phys. Rev. B **26**, 325 (1982).

[65] N. Nagaosa and Y. Tokura, Nat. Nanotechnol. **8**, 899 (2013).

[66] J. Liu, S. L. Zuo, H. Li, Y. L. Liu, X. Q. Zheng, Y. Zhang, T. Zhao, H. Fengxia, J. Sun, and B.-g. Shen, Scripta Mater. **187**, 268 (2020).

[67] X. Yu, Y. Tokunaga, Y. Taguchi, and Y. Tokura, Adv. Mater. **29**, 1603958 (2017).

[68] P. Zhang, A. Das, E. Barts, M. Azhar, L. Si, K. Held, M. Mostovoy, and T. Banerjee, Phys. Rev. Research **2**, 032026(R) (2020).

[69] W. F. Brown, Phys. Rev. **58**, 736 (1940).

[70] W. F. Brown, J. Phys. Radium **20**, 101 (1959).

[71] A. Vansteenkiste, J. Leliaert, M. Dvornik, M. Helsen, F. Garcia-Sanchez, and B. V. Waeyenberge, AIP Adv. **4**, 107133 (2014).

[72] M. A. Frantiu, Ph.D. thesis, University of Groningen, 2019.

[73] B. Göbel, A. Mook, J. Henk, I. Mertig, and O. A. Tretiakov, Phys. Rev. B **99**, 060407(R) (2019).

[74] W. Sun, W. Wang, H. Li, G. Zhang, D. Chen, J. Wang, and Z. Cheng, Nat. Commun. **11**, 5930 (2020).